

Structure of the multidrug resistance efflux transporter EmrE from *Escherichia coli*

Che Ma and Geoffrey Chang*

Department of Molecular Biology, The Scripps Research Institute, 10550 North Torrey Pines Road, CB-105, La Jolla, CA 92037

Communicated by Douglas C. Rees, California Institute of Technology, Pasadena, CA, January 7, 2004 (received for review November 13, 2003)

Multidrug resistance efflux transporters threaten to reverse the progress treating infectious disease by extruding a wide range of drug and other cytotoxic compounds. One such drug transporter, EmrE, from the small multidrug resistance family, utilizes proton gradients as an energy source to drive substrate translocation. In an effort to understand the molecular structural basis of this transport mechanism, we have determined the structure of EmrE from *Escherichia coli* to 3.8 Å. EmrE is a tetramer comprised of two conformational heterodimers related by a pseudo two-fold symmetry axis perpendicular to the cell membrane. Based on the structure and biochemical evidence, we propose a mechanism by which EmrE accomplishes multidrug efflux by coupling conformational changes between two heterodimers with proton gradient. Because of its simplicity and compact size, the structure of EmrE can serve as an ideal model for understanding the general structural basis of proton:drug antiport for other drug efflux systems.

The discovery and widespread use of antibiotics to control infectious disease has been one of the most important innovations of the 20th century. The increase of multidrug resistance (MDR) among pathogenic organisms in the last three decades has rendered many of these antibiotics useless (1, 2). As a result, several infectious diseases like tuberculosis, pneumonia, and gonorrhea have reemerged, causing an epidemic health problem affecting millions of people (3, 4). An important mechanism causing MDR involves the efflux of cytotoxic drug molecules by proteins embedded in the cell membrane known as MDR transporters. This class of integral membrane proteins is characterized by the extrusion of a broad range of substrates using energy-dependent mechanisms. Although critical for the health and defense of the cell, these transporters create significant problems in the chemotherapeutic treatment of many infectious diseases.

MDR transporters can be grouped into two major classes: MDR-ABC transporters that use the energy derived from the hydrolysis of ATP to drive substrate transport, and secondary MDR transporters, which use proton electrochemical gradients as the driving force (5, 6). Only few high-resolution structures of MDR transporters have been determined; this includes ABC transporter MsbA from *Escherichia coli* and *Vibrio cholerae* (7, 8), and secondary transporter AcrB from *E. coli* (9, 10). Among secondary MDR transporters, the small MDR (SMR) family has the simplest organization. Experiments probing the function of SMR transport systems have highlighted their importance and reveals that they are simple paradigms for understanding the mechanisms of drug transport coupled to proton gradients (11).

EmrE is a member of the SMR family (12) and belongs to the drug/metabolite transporter superfamily (13). The overexpression of EmrE causes bacteria to become resistant to wide variety of toxic cationic hydrophobic compounds such as ethidium bromide, methyl viologen, tetracycline, and tetraphenylphosphonium, as well as other antiseptics and intercalating dyes (14). EmrE is a proton:drug antiporter coupling substrate removal to electrochemical proton gradients in the opposite direction (15) and it is highly prevalent, with >60 homologs found in both Gram-positive and -negative bacteria (ref. 16 and Fig. 1). Being the smallest MDR transporter, EmrE from *E. coli* is a small

12-kDa protein with 110 amino acid residues and four predicted α -helices. EmrE is a hydrophobic protein with only eight charged residues, including Glu-14, which is conserved throughout the SMR family and is absolutely required for the drug efflux activity (17, 18). In *Bacillus subtilis*, homologs of EmrE are encoded by pairs of polypeptides (EbrA and EbrB, Fig. 1), suggesting that a heterooligomeric configuration is required for function (19, 20). EmrE structurally represents the most basic of MDR transporters and is, therefore, an ideal candidate for understanding the molecular basis underlying the antiport mechanism. The structure of EmrE determined to 3.8 Å provides a framework for understanding the structural basis coupling drug transport with proton flux.

Materials and Methods

Purification and Crystallization. EmrE homologs were cloned into a modified pET15b expression vector (Novagen), which includes a fusion peptide containing an NH₃-terminal deca- or hexahistidine tag. Clones were expressed in *E. coli* host BL21(DE3) (Novagen) in an 80-l batch fermentor at 37°C by using 2 mM isopropyl β -D-thiogalactopyranoside as an inducer. EmrE protein was extracted from 200 grams of *E. coli* by agitation in the presence of 2% *N*-nonyl- β -D-glucopyranoside (NG). Extracted EmrE was purified in the presence of 20 mM Tris·HCl (pH 8.0)/20 mM NaCl/0.3% NG by using nickel-chelating, ion-exchange, and gel-filtration chromatography. The histidine tag was removed by proteolytic cleavage by thrombin. Purified EmrE proteins were assayed for purity by Coomassie blue staining SDS/PAGE, was confirmed by MS, and was then concentrated to 10–15 mg/ml.

Crystallization trials were performed by using a multivariate crystallization matrix of temperatures, detergents, precipitants, salts, and additives. *E. coli* EmrE crystals were obtained by using the vapor diffusion hanging-drop method at 4°C, by combining protein with precipitant at a ratio of 2–3:1. The precipitant solution contained 20 mM NaCl, 20 mM sodium acetate (pH 4.0), 200–600 mM ammonium sulfate, 15–30% polyethylene glycol 200, and 0.3–0.6% NG. Crystals appeared within five days and continued to grow for two weeks to a full size of 0.3 × 0.4 × 0.4 mm. To verify identity, crystals were washed, dissolved, and analyzed by SDS/PAGE. MS analysis also confirmed its predicted molecular weight.

Data Collection and Structure Determination. Anomalous difference data collected near the Hg LIII edge ($\lambda = 1.00674$ Å) and inflection point ($\lambda = 1.00879$ Å) from Hg-derivatized EmrE mutant C41S crystals was applied to calculate the Hg substructure by using the program SNB yielding 16 sites (21). The position of Cys-41 was determined by cross difference Fourier with the anomalous data from the wild-type crystal (giving 24 Hg sites)

Abbreviations: MDR, multidrug resistance; SMR, small MDR; NG, *N*-nonyl- β -D-glucopyranoside.

Data deposition: The atomic coordinates have been deposited in the Protein Data Bank, www.pdb.org (PDB ID code 157B).

*To whom correspondence should be addressed. E-mail: gchang@scripps.edu.

© 2004 by The National Academy of Sciences of the USA

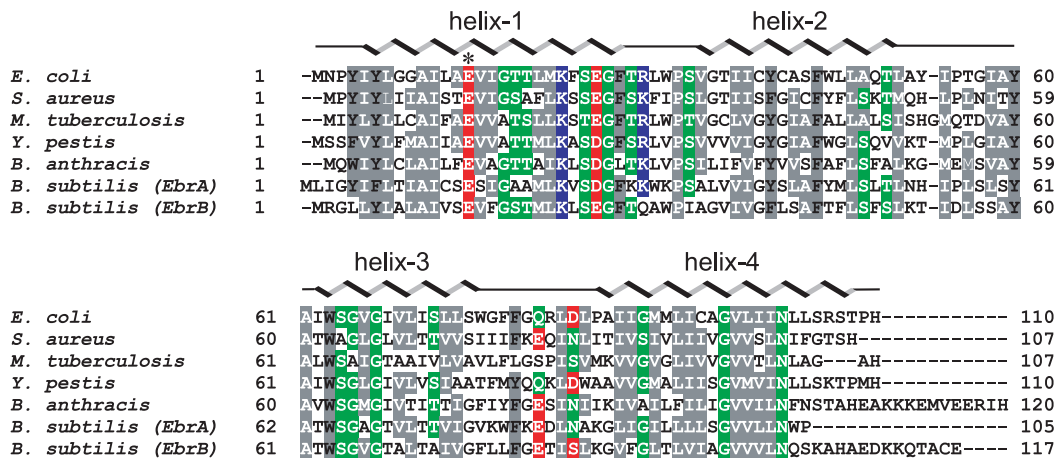


Fig. 1. Amino acid sequence alignment of EmrE from *E. coli* shown with other homologs from human pathogens produced by using the program CLUSTALW (59). Conserved residues are colored according to their acidic (red), basic (blue), polar (green), or hydrophobic (gray) character. The α -helices from the EmrE crystal structure are indicated, as well as the position of Glu-14, by an asterisk. The following National Center for Biotechnology Information accession codes were used for the alignment: *E. coli*, NP_415075; *Staphylococcus aureus*, NP_863640; *Mycobacterium tuberculosis*, NP_217581; *Bacillus anthracis*, NP_657212; *Yersinia pestis*, NP_405870; and *Bacillus subtilis*, NP_389612 and NP_389611.

and protein phases were combined by using the software package PHASES (22). The initial experimentally phased electron density maps revealed that there are two tetramers in the asymmetric unit with each half of the tetramer containing a conformational heterodimer of EmrE monomers. Four-fold noncrystallographic symmetry averaging, solvent flattening, and incremental phase extension from 4.5- to 3.8-Å resolution were accomplished by using locally written programs (G.C., unpublished work) to yield electron density maps for model building. MS analysis indicated that the mass of the crystal consisted only of full-length EmrE protein, NG, mercury, and solvent components. A chemical model was built by using the programs CHAIN (23) and O (24). Vector refinement by using averaged phases was accomplished by using the program X-PLOR (25) to best fit the model into the experimental electron density map.

Results and Discussion

Structure Determination of EmrE. The crystallization of integral membrane proteins is a challenge, which is due mainly to their amphipathic nature. Finding the optimal detergent and protein combinations for crystallization is an important key (26). To obtain well diffracting crystals of EmrE, we explored crystallization space by cloning, expressing, and purifying nine EmrE

homologs from seven prokaryotic species, with the anticipation that the natural sequence variations between the homologs would increase the likelihood for crystal formation. Four EmrE homologs were found to have significantly higher protein expression levels by using *E. coli* BL21 strains. After screening and refining crystallization conditions in combination with 15 detergents, EmrE crystals from *E. coli* were found to be of good diffracting quality and were used for x-ray structure analysis.

Native crystals of EmrE grew in space group F222 with cell dimensions ($a = 178.7 \text{ \AA}$, $b = 235.3 \text{ \AA}$, $c = 288.2 \text{ \AA}$) and diffracted to $\approx 5 \text{ \AA}$. In an effort to improve the diffraction quality of these crystals, we used a strategy of soaking the crystals with hundreds of additives and heavy-atom compounds to stabilize the lattice interactions (27). During the course of these trials, we identified several mercurial compounds that improved the diffraction quality of these crystals to a resolution limit of 3.8 Å (Tables 1 and 2). The anomalous difference Pattersons from these crystals, however, were difficult to interpret because of the large number of heavy-atom sites and resolution limit. Because biochemical studies of EmrE strongly suggested that residues Cys-39, Cys-41, and Cys-95 could react with mercurial compounds (28), we cloned and purified 25 different EmrE mutants replacing either one or two of the cysteines with conserved

Table 1. Crystallographic analysis

	Crystal 1 HgCl ₂ Peak/Inflection	Crystal 2 (CH ₃) ₂ Hg Peak/Inflection	Crystal 3 HgCl ₂ Peak/Inflection	Crystal 4 HgCl ₂ Peak/Inflection	Crystal 5 HgCl ₂
Diffraction data					
Beamline	SSRL BL11-1	SSRL BL9-2	ALS BL5.0.2	APS BC14-ID-B	APS BC14-ID-B
Wavelength, Å	1.00570/1.00894	1.00567/1.00883	1.00720/1.00940	1.00674/1.00879	1.00674
Bragg spacing limits, Å	40–4.2/40–4.5	40–4.2/40–4.2	40–4.5/40–4.8	40–4.0/40–4.0	40–3.8
Total/unique observations	20,792/16,883	21,452/21,219	18,906/14,553	25,798/25,611	34,398
Redundancy	3.4/3.4	3.3/3.3	3.4/3.4	3.5/3.5	7.2
Completeness, %	86.6/87.0	95.3/95.1	90.1/87.4	99.2/98.5	90.0
R _{sym} , %	7.4/5.7	8.8/8.2	8.2/7.1	10.4/8.6	10.2

X-ray diffraction data and multiwavelength anomalous diffraction phases for EmrE crystals were screened and collected at the Stanford Synchrotron Radiation Laboratory (Beamline 11-1, 9-1, 9-2), the Advanced Light Source (Beamline 5.0.2, 8.2.1, 8.2.2), and the Advanced Photon Source (BioCARS 14-ID-B). Crystals 1, 2, and 3 are from wild-type EmrE. Crystals 4 and 5 are C415 mutant and have similar unit cell dimensions to the wild-type crystals. All data sets were collected at 100 K and were processed by using the programs HKL2000 (HKL Research). In all cases, soaking the crystals with either HgCl₂, (CH₃)₂Hg, (CH₃)HgCl, (CH₃CH₂)HgCl, and (CH₃)HgPO₄ significantly increased the diffraction resolution of both the wild-type and C415 crystals. The features of the anomalous Patterson's were the same soaking with any of these mercurial compounds.

Table 2. Generation of experimental electron density, refinement statistics, and model geometry

Generation of experimental electron density	
Average phasing power for any data set	2.8
Average initial density correlation between the four structural heterodimers	55%
Overall figure of merit	0.58
Refinement statistics	
R factor/ R_{free} , % (40.0–3.8 Å)	32/35
Overall B factor of the model, Å ²	55
Model geometry	
Bond length deviation, Å	0.01
Bond angle deviation, °	1.5

residues found at that position in other homologs. Only one mutant, C41S, crystallized, and the mercury sites were identified by using the dual space direct methods SNB algorithm (ref. 21 and Fig. 2A). Initial electron density maps indicated that the asymmetric unit contained eight monomers, corresponding to a relatively high Matthews coefficient (29) of ≈ 7.8 Å³/Da and a solvent/detergent content of $\approx 84\%$. Iterative noncrystallographic averaging, solvent flattening, and phase-extension produced electron density maps for model building (Fig. 2C). The protein sequence registration of the model was first established by the mercury locations in the electron density maps corresponding to cysteine positions 39, 41, and 95 (Fig. 2B), and then later confirmed by the bulky side-chain positions in the sequence (Fig. 2C). The structure was refined with a crystallographic $R_{\text{cryst}}/R_{\text{free}}$ of 0.32/0.35. The relatively higher values of the $R_{\text{cryst}}/R_{\text{free}}$ reflect the rapid decrease of the diffraction intensities as a function of resolution, the anisotropy of the data, and the presence of semiordered parts of NG molecules surrounding the transmembrane portions of the molecule that were not included in the refinement calculations. We estimate that at least 30% of the total scattering from the crystal is contributed from these partially ordered detergent molecules. A chemical model was built with good geometry and no residues in disallowed regions of the Ramachandran plot.

Structural Organization of EmrE. The structure of EmrE reveals a tetramer composed of two conformational heterodimers related by a pseudo two-fold symmetry axis perpendicular to the membrane surface (Fig. 3A). In the heterodimer, helices-1, -2, and -3 from one subunit are arranged in an approximately inverted orientation relative to the other monomer, forming a six-helix bundle with a hydrophobic core. Fig. 3B shows the superposition of the two distinct conformations adopted by EmrE subunits. Whereas helix-1, helix-2, and part of helix-3 show considerable agreement at their C α positions (1.08-Å rms deviation between helix-1 and -2), helix-4 within the heterodimer shows significant deviation from each other. Whereas helix-4 from one subunit is nearly parallel to the membrane surface, the other is protruding through the plane of the membrane. The position of helix-4 at the outer membrane leaflet side of the lipid bilayer is consistent with biochemical studies, suggesting interaction of a sulfhydryl-reactive reagent with Cys-95 only from the outer surface of the membrane (30). Other membrane topology evidence suggests that helix-4 could be transmembrane possibly in another state of the molecule (28). The lateral positioning of helix-4 along the surface of the cell membrane seen in this structure has been observed in several other membrane proteins, such as the E and M membrane proteins of the flavivirus (31).

One of the most intriguing features of the EmrE structure is the inverted orientation of polypeptides forming the conformational heterodimers. Although unprecedented, this conformational arrangement gives merit to possible gene-fusion events

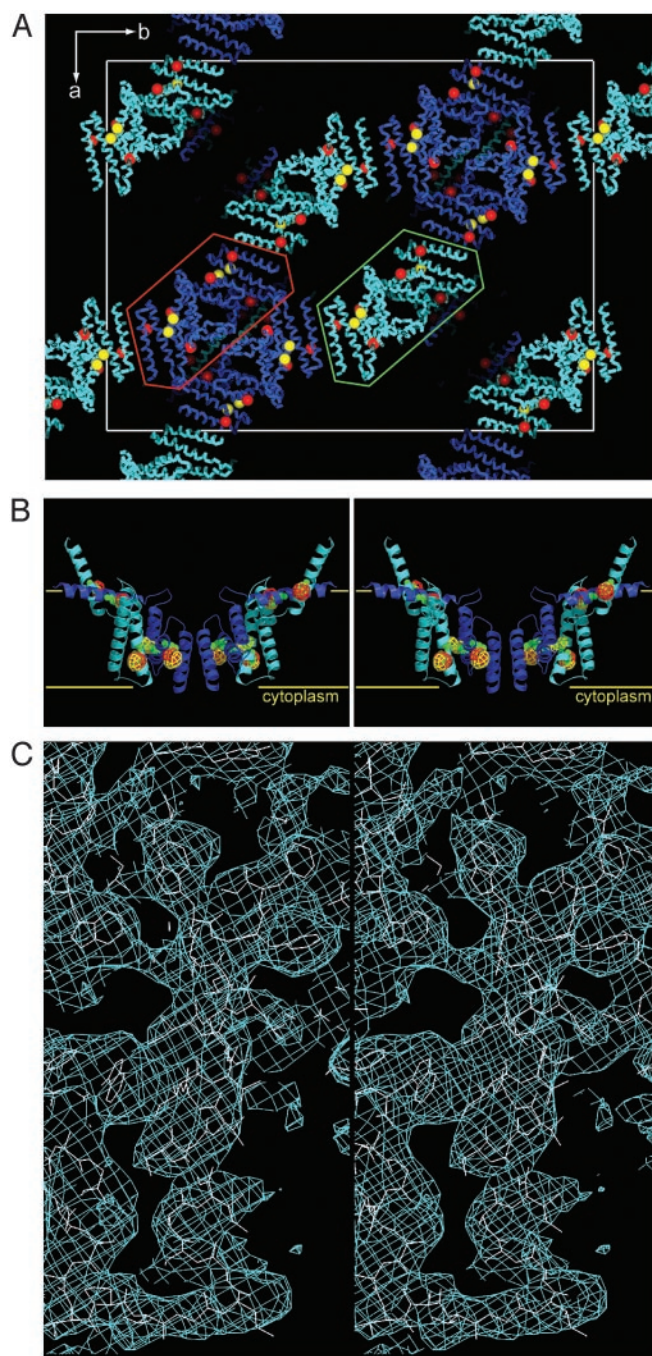


Fig. 2. Structure determination of EmrE. (A) Packing diagram of the EmrE drug transporter in the crystal. The space group is F222. The red spheres indicate the positions of mercury bound to Cys-39 and Cys-95. Yellow spheres indicate the additional mercury site at Cys-41 obtained from the wild-type anomalous data. The two EmrE tetramers, related by noncrystallographic symmetry, are enclosed by green and red lines. (B) Stereoview of the EmrE structure with anomalous difference density by using model phases for mercury at Cys-39 and Cys-95 (red) and Cys-41 (yellow). The positions of cysteine residues are indicated by green spheres. The lipid bilayer is represented with yellow horizontal lines separated by ≈ 35 Å. (C) Stereoview of experimental electron density for helix-3. The density is contoured at 1σ .

producing other transporters such as drug/metabolite exporters in the drug/metabolite transporter superfamily, whose homologous subunits are thought to be inverted in the lipid bilayer (13). Indeed, this type of fusion is supported by structures such as the

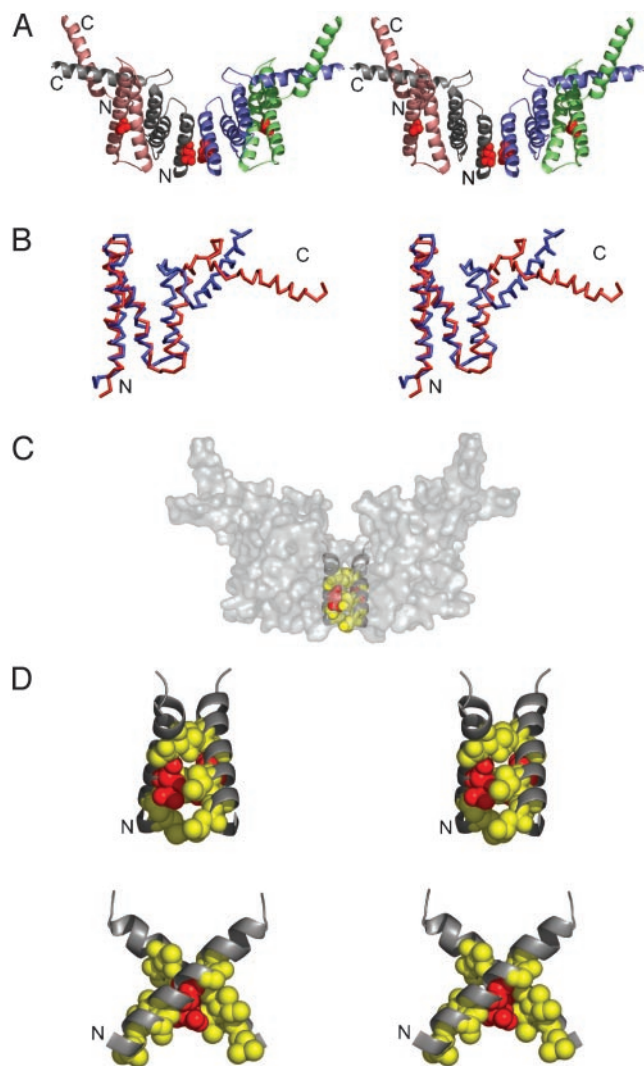


Fig. 3. Structure of EmrE. (A) Side stereoview of EmrE. EmrE is a tetramer composed of two structural heterodimers. Each heterodimer contains subunits with different conformations. NH₃ and COOH termini are indicated. The residue Glu-14 is shown in red spheres. (B) Stereoview of superimposed C α traces of subunits of the structural heterodimer are red and blue. (C) Surface representation of EmrE highlighting the drug translocation pathway. (D) Stereoview close-ups of the pair of Helix-1s at the interface between structural heterodimers are shown with black ribbons. Residues that abolish EmrE activity when replaced with cysteines are indicated with red spheres for Glu-14 and yellow for Leu-7, Ala-10, Ile-11, Gly-17, and Thr-18. All figures were prepared by using the programs PYMOL (www.pymol.org) or VMD (60) and were rendered with POV-RAY (www.povray.org).

chloride channel (32), aquaporins (33), and the vitamin ABC transporter BtuCD (34), which have inverted transmembrane subdomains encoded in a single polypeptide. In the case of EmrE structure, there is the potential to fuse the C terminus of helix-4 of one monomer with the N terminus of another monomer within the asymmetric dimer. This observation may explain how transmembrane subunits of other evolutionarily later transporters and channels are formed.

In this structure, the tetramer is formed from contacts of helix-1 from both heterodimers with a crossing angle of $\approx 90^\circ$. The buried surface area is $\approx 550 \text{ \AA}^2$, which is consistent with the relatively small size of EmrE and may reflect the conformational state trapped by this crystal form. The open conformation of MsbA, for example, is a much larger MDR transporter and

buries 850 \AA^2 between the two halves of the dimer (7). Located at this juncture are a pair of functionally important Glu-14s and several residues important for substrate and proton binding (ref. 35 and Fig. 3C). This membrane-embedded glutamate is required for substrate binding, and its protonation state is believed to play a crucial role in the mechanism by which proton gradients are used to remove cationic hydrophobic drugs (36, 37). The X-shape arrangement from this pair of helix-1s (Fig. 3D), and the positions of the glutamate residues at the pivot point is consistent with previous studies, demonstrating that Glu-14 is the only residue in helix-1 that can be cross-linked by HgCl₂ when replaced with cysteine (41). In addition, site-directed spin-labeling studies (38) also suggest that Glu-14s are in close proximity and predict a scissors-like two-fold symmetric spatial organization of both opposing helix-1s. Taken together with the available biochemical evidence, we propose that this interface is likely to be the drug translocation pathway.

Oligomerization State of EmrE. The tetrameric arrangement of EmrE in the crystal structure is in contrast with earlier studies (39–41) suggesting that EmrE is a trimer or solely a heterodimer configuration, whereas other studies were inconclusive on this point. Recent cryo-electron microscopy studies (42–44) revealed a 7- \AA resolution structure of EmrE suggesting that EmrE exists as an asymmetric dimer, but did not rule out that *in vivo* the functional unit is a tetramer composed of two asymmetric dimers. A recent review on the quaternary structure of transporters interpreting the same biochemical and electron microscopy data concluded that EmrE is likely a dimer of dimers or a tetramer (45). We observed that EmrE migrates as a tetramer with an apparent molecular weight of $\approx 48 \text{ kDa}$ by using gel-filtration chromatography analysis. EmrE is 90% retained by using a 100-kDa cut-off membrane when concentrated, which agrees well with the estimated size of a tetramer/NG micelle complex. In addition, a recently identified archaeal homolog of EmrE migrates both as a dimer and tetramer on SDS/PAGE (46). We believe that the interaction of helix-1s between asymmetric dimers in our crystal, which is supported by site-directed spin labeling and cross-linking studies, is compatible with a tetramer (dimer of dimers) as the molecular unit. Furthermore, we have two copies of this molecular unit in the unit cell packed in two distinctly different ways, as indicated in Fig. 2. Although not unequivocal, the experimental evidences taken together with the x-ray data suggest the possibility that EmrE could associate to form a tetramer.

Proposed Drug-Efflux Mechanism. First identified nearly a decade ago (47), EmrE has been the subject of extensive characterizations by molecular biological and biophysical techniques because of its relatively small size and simple configuration. Many questions, however, remain unanswered. How does a polypeptide with 110 amino acid residues and only one indispensable charged residue, Glu-14, accomplish such a complex task, coupling a proton gradient with multidrug efflux? We suggest a general mechanism for the cationic hydrophobic substrate translocation based on our crystal structure and biochemical evidence, emphasizing that Glu-14 not only plays a crucial role in the binding of the cationic hydrophobic substrates but also couples the proton electromotive force driving substrate translocation (Fig. 4). In our structure, we observe two pairs of Glu-14 residues: one set is situated near the proposed drug-binding pathway at the interface between structural heterodimers and a second set located near the exterior of the protein closer to the outer membrane side (red spheres, Fig. 4). Although chemically indistinguishable by biophysical or genetic methods, these residues are in structurally nonequivalent positions and are likely to have different roles. Both glutamate positions, however, are functionally important, because they are absolutely conserved

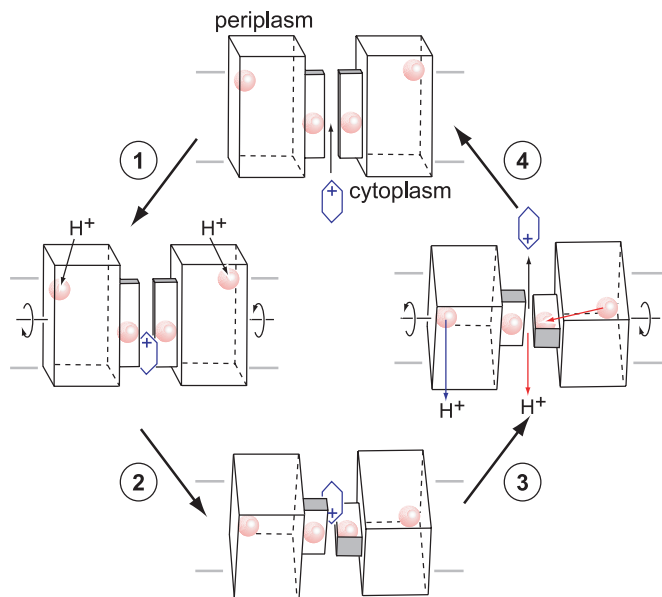


Fig. 4. Proposed drug-efflux mechanism by EmrE. Stages 1–4 begin at the top and proceed counterclockwise. See text for details. 1, Cationic hydrophobic substrate bind to Glu-14s (red spheres) located near the drug translocation pathway when EmrE is in the high-affinity state for binding drugs. Helix-1 is represented by a smaller rectangular box along this pathway. 2, Protonation of Glu-14s near the extracellular surface triggers a conformational change in the relative positioning of the structural heterodimers. 3, Protons are released into the cytoplasm by two possible pathways shown in blue and red. Substrate is ejected to the periplasm. 4, EmrE returns to its drug-binding state and the transport cycle is reset. The cell membrane is represented as a set of two horizontal lines. The Glu-14 positions and the substrate are represented by red spheres and a blue hexagonal ring, respectively. In this high-affinity state, the tilt angle of the helices relative to the membrane normal could be as much as 27° , as suggested from Fourier transform infrared studies of EmrE (61).

even among EmrE homologs that function only as heterooligomers such as YkkCD and EbrAB (48). The role of charged residues mediating proton translocation has been observed in several proton pumps such as light-driven bacteriorhodopsin (49, 50), subunit c of the F_1F_0 ATPase (51, 52), and photosynthetic complexes (53). In the lactose permease, a glutamate residue residing near the extracellular side of the cell membrane is first protonated, and then this proton transfers to another glutamate positioned during lactose translocation. We propose that the inside set of Glu-14 residues in EmrE is responsible for substrate binding, and the outside set serves as proton sensors initiating the transport cycle when EmrE is in the high-affinity state for binding drugs.

In the high-affinity state (shown as a model in step 1, Fig. 4), the drug-binding Glu-14s carry negative charge and can bind cationic hydrophobic substrates from either the cytoplasm or from the inner membrane leaflet side of the cell membrane. Drug binding is stabilized by electrostatic and hydrophobic interactions from neighboring residues (Glu-14, Leu-7, Ala-10, Ile-11, Gly-17, and Thr-18). In the presence of an electromotive force, the Glu-14s located near the cell surface are protonated causing a conformational change that is propagated through the heterodimer, “rocking” both halves of the tetramer into a position with a crossing angle of $\approx 90^\circ$. This movement presents the substrate to the periplasmic side of the cell membrane and forms a closed juncture that is observed in our structure preventing the substrate from going back into the cytoplasm (step 2, Fig. 4). The proposed counterrotational movement interconverting the two drug-binding states is substantiated by significant positional differences ($>3.2 \text{ \AA}$ in the C^α position) observed

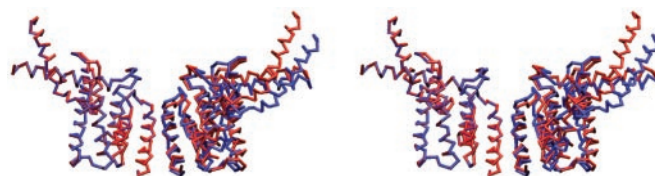


Fig. 5. Stereoview highlighting the positional differences between noncrystallographic equivalent tetramers. The C^α superposition aligning a heterodimer from each tetramer reveals significant displacement on the other half.

between heterodimers of noncrystallographic equivalent tetramers (Fig. 5). In the low-affinity drug-binding state, the neutral proton-sensing Glu-14s are located in the cell membrane interior in an energetically favorable position.

The exact pathway of protons passing through EmrE to the cytoplasm is not clear. In one possible mechanism, these protons are ejected directly into the cell interior (blue arrow, step 3, Fig. 4) by some unknown pathway, and the transport system simply resets to the high-affinity state for binding drugs. Another more striking possibility involves the passage of protons through the hydrophobic core of the heterodimer, allowing the protonation of the drug-binding Glu-14s, causing drug release (red arrow, step 3, Fig. 4). The distance between the inner and outer glutamates within an asymmetric dimer is $\approx 32 \text{ \AA}$. This mechanism would effectively couple the release of substrate with the proton motive force, completing the antiport mechanism. The deprotonation of external Glu-14s would cause the transporter to energetically favor the high-affinity state for binding drugs, thereby resetting the system (step 4, Fig. 4).

Conclusion

The crystal structure of EmrE reveals the organization of a compact integral membrane protein and provides a detailed framework for understanding the mechanism coupling the proton motive force with drug transport across the cell membrane. Although this particular conformation of EmrE does not fully explain all of the published biochemical observations, the structure is compatible with several experimental evidences. In general, biochemical studies of EmrE have identified important residues that are critical for drug binding and proton translocation. However, additional observations of the x-ray structure suggest that the positions of the functionally important Glu-14 residues are different, and that the transporter is likely to undergo significant conformational change, both on the quaternary and monomeric level. Together with the large structural flexibilities inherent in MDR transporters, which are necessary to accommodate the passage of relatively bulky hydrophobic substrates, movements in transmembrane α -helices through the transport cycle may confound attempts to unambiguously identify helix–helix interactions through biochemical studies such as cross-linking. The importance of these structural elements as well as large conformational changes within the structure during the transport cycle are emphasized by the role that these features have been proposed to play by the potassium ion channels and the acetylcholine receptors (54–56).

Compared with the structures of the lactose permease (57) and the glycerol-3-phosphate transporter (58), the structure of EmrE is unusual, having an X shape formed from two crossing α -helices instead of a pore-like structure. This arrangement, however, is perfectly consistent with the function of EmrE as a MDR transporter, accepting hydrophobic substrates from the inner membrane leaflet of the lipid bilayer. Like the structures of the MDR-ABC transporter homolog MsbA, the V-shaped structure is probably a general feature of multidrug/lipid transporters, which are postulated to act as “flippases,” moving

substrate from the inner to the outer cell membrane or extruding them to the external milieu of the cell. Clearly, more structures from different states of EmrE will further clarify the mechanism of drug binding and substrate transport.

We thank the staff at the Advanced Light Source, the Stanford Synchrotron Radiation Laboratory, and the Advanced Photon Source for their assistance with the screening of crystals and x-ray data collection; P. Wright, J. Kelly,

and R. Lerner for supporting membrane protein x-ray crystallography at The Scripps Research Institute; D. C. Rees for many thoughtful discussions and careful reading of the manuscript; and P. Wright, J. Dyson, R. Milligan, I. Wilson, R. Spencer, O. Pornillos, C. Reyes, Y. Yin, T. H. Huang, and S. Wada for discussions. This work was supported by National Institutes of Health Grant GM067644, a Beckman Young Investigator Award, National Aeronautics and Space Administration Grant NAG8-1834, the Skaggs Foundation for Chemical Biology, and the Presidential Early Career Award for Scientists and Engineers.

1. Neu, H. C. (1992) *Science* **257**, 1064–1073.
2. Moellering, R. C. (1998) *Clin. Infect. Dis.* **26**, 1177–1178.
3. Levy, S. B. (1992) *Antimicrob. Agents Chemother.* **36**, 695–703.
4. Levy, S. B. (1998) *Sci. Am.* **278**, 46–53.
5. Gottesman, M. M. & Pastan, I. (1993) *Annu. Rev. Biochem.* **62**, 385–427.
6. Paulsen, I. T., Brown, M. H. & Skurray, R. A. (1996) *Microbiol. Rev.* **60**, 575–608.
7. Chang, G. & Roth, C. B. (2001) *Science* **293**, 1793–1800.
8. Chang, G. (2003) *J. Mol. Biol.* **330**, 419–430.
9. Murakami, S., Nakashima, R., Yamashita, E. & Yamaguchi, A. (2002) *Nature* **419**, 587–593.
10. Yu, E. W., McDermott, G., Zgurskaya, H. I., Nikaido, H. & Koshland, D. E., Jr. (2003) *Science* **300**, 976–980.
11. Schuldiner, S., Lebendiker, M. & Yerushalmi, H. (1997) *J. Exp. Biol.* **200**, 335–341.
12. Paulsen, I. T., Skurray, R. A., Tam, R., Saler, M. H., Turner, R. J., Weiner, J. H., Goldberg, E. B. & Grinius, L. L. (1996) *Mol. Microbiol.* **19**, 1167–1175.
13. Jack, D. L., Yang, N. M. & Saier, M. H. (2001) *Eur. J. Biochem.* **268**, 3620–3639.
14. Yerushalmi, H., Lebendiker, M. & Schuldiner, S. (1995) *J. Biol. Chem.* **270**, 6856–6863.
15. Grinius, L. L. & Goldberg, E. B. (1994) *J. Biol. Chem.* **269**, 29998–30004.
16. Schuldiner, S., Granot, D., Mordoch, S. S., Ninio, S., Rotem, D., Soskin, M., Tate, C. G. & Yerushalmi, H. (2001) *News Physiol. Sci.* **16**, 130–134.
17. Yerushalmi, H. & Schuldiner, S. (2000) *J. Biol. Chem.* **275**, 5264–5269.
18. Yerushalmi, H., Mordoch, S. S. & Schuldiner, S. (2001) *J. Biol. Chem.* **276**, 12744–12748.
19. Masaoka, Y., Ueno, Y., Morita, Y., Kuroda, T., Mizushima, T. & Tsuchiya, T. (2000) *J. Bacteriol.* **182**, 2307–2310.
20. Jack, D. L., Storms, M. L., Tchieu, J. H., Paulsen, I. T. & Saier, M. H. (2000) *J. Bacteriol.* **182**, 2311–2313.
21. Miller, R., Gallo, S. M., Khalak, H. G. & Weeks, C. M. (1994) *J. Appl. Crystallogr.* **27**, 613–621.
22. Furey, W. & Swaminathan, S. (1997) *Methods Enzymol.* **277**, 590–620.
23. Sack, J. S. (1988) *J. Mol. Graphics* **6**, 224–225.
24. Jones, T. A., Zou, J. Y., Cowan, S. W. & Kjeldgaard, M. (1991) *Acta Crystallogr. A* **47**, 110–119.
25. Brunger, A. T. (1992) *X-PLOR, Version 3.1. A System for X-ray Crystallography and NMR* (Yale Univ. Press, New Haven, CT).
26. Ostermeier, C. & Michel, H. (1997) *Curr. Opin. Struct. Biol.* **7**, 697–701.
27. Chang, G., Spencer, R. H., Lee, A. T., Barclay, M. T. & Rees, D. C. (1998) *Science* **282**, 2220–2226.
28. Mordoch, S. S., Granot, D., Lebendiker, M. & Schuldiner, S. (1999) *J. Biol. Chem.* **274**, 19480–19486.
29. Matthews, B. W. (1968) *J. Mol. Biol.* **33**, 491–497.
30. Lebendiker, M. & Schuldiner, S. (1996) *J. Biol. Chem.* **271**, 21193–21199.
31. Zhang, W., Chipman, P. R., Corver, J., Johnson, P. R., Zhang, Y., Mukhopadhyay, S., Baker, T. S., Strauss, J. H., Rossmann, M. G. & Kuhn, R. J. (2003) *Nat. Struct. Biol.* **10**, 907–912.
32. Dutzler, R., Campbell, E. B., Cadene, M., Chait, B. T. & MacKinnon, R. (2002) *Nature* **415**, 287–294.
33. Cheng, A. C., vanHoek, A. N., Yeager, M., Verkman, A. S. & Mitra, A. K. (1997) *Nature* **387**, 627–630.
34. Locher, K. P., Lee, A. T. & Rees, D. C. (2002) *Science* **296**, 1091–1098.
35. Gutman, N., Steiner-Mordoch, S. & Schuldiner, S. (2003) *J. Biol. Chem.* **278**, 16082–16087.
36. Yerushalmi, H. & Schuldiner, S. (2000) *Biochemistry* **39**, 14711–14719.
37. Yerushalmi, H. & Schuldiner, S. (2000) *FEBS Lett.* **476**, 93–97.
38. Koteiche, H. A., Reeves, M. D. & McHaourab, H. S. (2003) *Biochemistry* **42**, 6099–6105.
39. Yerushalmi, H., Lebendiker, M. & Schuldiner, S. (1996) *J. Biol. Chem.* **271**, 31044–31048.
40. Muth, T. R. & Schuldiner, S. (2000) *EMBO J.* **19**, 234–240.
41. Soskine, M., Steiner-Mordoch, S. & Schuldiner, S. (2002) *Proc. Natl. Acad. Sci. USA* **99**, 12043–12048.
42. Tate, C. G., Kunji, E. R. S., Lebendiker, M. & Schuldiner, S. (2001) *EMBO J.* **20**, 77–81.
43. Tate, C. G., Ubarretxena-Belandia, I. & Baldwin, J. M. (2003) *J. Mol. Biol.* **332**, 229–242.
44. Ubarretxena-Belandia, I., Baldwin, J. M., Schuldiner, S. & Tate, C. G. (2003) *EMBO J.* **22**, 6175–6181.
45. Veenhoff, L. M., Heuberger, E. & Poolman, B. (2002) *Trends Biochem. Sci.* **27**, 242–249.
46. Ninio, S. & Schuldiner, S. (2003) *J. Biol. Chem.* **278**, 12000–12005.
47. Grinius, L., Dreguniene, G., Goldberg, E. B., Liao, C. H. & Projan, S. J. (1992) *Plasmid* **27**, 119–129.
48. Chung, Y. J. & Saier, M. H. (2001) *Curr. Opin. Drug Discov. Devel.* **4**, 237–245.
49. Lanyi, J. K. (1993) *Biochim. Biophys. Acta* **1183**, 241–261.
50. Lanyi, J. K. (1999) *FEBS Lett.* **464**, 103–107.
51. Miller, M. J., Oldenburg, M. & Fillingame, R. H. (1990) *Proc. Natl. Acad. Sci. USA* **87**, 4900–4904.
52. Rastogi, V. K. & Girvin, M. E. (1999) *Nature* **402**, 263–268.
53. Paddock, M. L., Rongey, S. H., McPherson, P. H., Juth, A., Feher, G. & Okamura, M. Y. (1994) *Biochemistry* **33**, 734–745.
54. Jiang, Y. X., Lee, A., Chen, J. Y., Ruta, V., Cadene, M., Chait, B. T. & MacKinnon, R. (2003) *Nature* **423**, 33–41.
55. Jiang, Y. X., Ruta, V., Chen, J. Y., Lee, A. & MacKinnon, R. (2003) *Nature* **423**, 42–48.
56. Miyazawa, A., Fujiyoshi, Y. & Unwin, N. (2003) *Nature* **423**, 949–955.
57. Abramson, J., Smirnova, I., Kasho, V., Verner, G., Kaback, H. R. & Iwata, S. (2003) *Science* **301**, 610–615.
58. Huang, Y., Lemieux, M. J., Song, J., Auer, M. & Wang, D. N. (2003) *Science* **301**, 616–620.
59. Thompson, J. D., Higgins, D. G. & Gibson, T. J. (1994) *Nucleic Acids Res.* **22**, 4673–4680.
60. Humphrey, W., Dalke, A. & Schulten, K. (1996) *J. Mol. Graphics* **14**, 33–38.
61. Arkin, I. T., Russ, W. P., Lebendiker, M. & Schuldiner, S. (1996) *Biochemistry* **35**, 7233–7238.